Finite-size effects in metasurface lasers based on resonant dark states

Sotiris Droulias[1*], Thomas Koschny[2] and Costas M. Soukoulis[1,2]

[1]*Institute of Electronic Structure and Laser, FORTH, 71110 Heraklion, Crete, Greece*
[2]*Ames Laboratory and Department of Physics and Astronomy, Iowa State University, Ames, Iowa 50011, USA*
**e-mail: sdroulias@iesl.forth.gr*

Supplementary Material

1. Calculation of *Q* factors and additional information on *Q* factor tunability (system suspended in air)

Our system is examined with full-wave vectorial Finite Element Method (FEM) eigenfrequency simulations, utilizing the commercial software COMSOL Multiphysics. In order to identify the eigenmodes of the system and their respective Q factors, in all calculations the system is assumed to be unpumped. For a mode with eigenfrequency ω, the Q factor is defined as $Q = \omega \frac{W_{stored}}{P_{diss} + P_{rad}}$, where W_{stored} is the energy stored in the mode, P_{diss} the dissipated power (due to material absorption) and P_{rad} the radiated power (due to leakage and/or outcoupling in the presence of the scatterer). Separating the contribution of each loss channel into $Q_{diss} = \omega \frac{W_{stored}}{P_{diss}}$ and $Q_{rad} = \omega \frac{W_{stored}}{P_{rad}}$, the total Q factor can be written as $Q_{total}^{-1} = Q_{diss}^{-1} + Q_{rad}^{-1}$ (the subscript 'total' has been introduced for emphasis). To calculate the necessary quantities W_{stored}, P_{diss} and P_{rad} for the evaluation of Q_{total}, Q_{diss} and Q_{rad} we calculate the eigenmodes of a certain system. The computational space is terminated by Perfectly Matched Layer (PML) and the simulation provides us with the field profile of each mode, as well as with the complex eigenfrequency $\omega = 2\pi f$ (simulation eigenvalue), which expresses the dissipative and radiative losses. Hence, the total Q factor can be alternatively calculated directly from the complex eigenfrequency as $Q_{total} = \mathrm{Re}(\omega)/2\mathrm{Im}(\omega)$, consistently with the definition. While P_{diss} and P_{rad} are integrated directly on the relevant areas, the calculation of W_{stored} introduces some ambiguity, due to the non-strict boundaries of the dark mode when it is coupled to radiating waves. However, this ambiguity is lifted by using the calculated Q_{total} from the eigenfrequency. Then, the separate quantities are given by: $Q_{diss} = Q_{total} \frac{P_{diss} + P_{rad}}{P_{diss}}$ and $Q_{rad} = Q_{total} \frac{P_{diss} + P_{rad}}{P_{rad}}$.

In Fig. 3 the competition between outcoupling from the scatterer and leakage was shown, via the calculated Q_{diss}, Q_{rad} and Q_{total}. As mentioned, leakage depends on the system size only and outcoupling from the scatterer on the scatterer strength. There, for illustration purposes, a certain scatterer was chosen to have a 30nm × 60nm rectangular cross section and permittivity 12.1, leading to a certain minimum value for the Q_{scat}. Here we examine further this competition for other scatterer strengths, by keeping the scatterer geometry and changing its permittivity. Fig. S1.A.c is reproduced from Fig.3 for easier comparison.

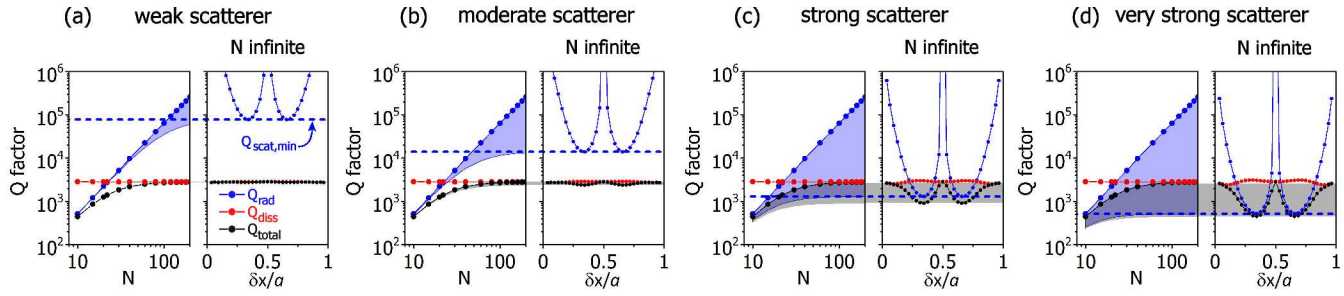

Figure S1.A: *Q* factor tunability for different scatterer strengths, in the presence of leakage. The scatterer has a 30nm × 60nm rectangular cross section and permittivity $\varepsilon_{r,scat} = 2.5$ in (a), $\varepsilon_{r,scat} = 4.5$in (b), $\varepsilon_{r,scat} = 12.1$ in (c) and $\varepsilon_{r,scat} = 18$ in (d). The blue-shaded area denotes the Q_{rad} tunability region and the grey-shaded area denotes the total Q tunability region.

For weak scatterer, in particular, it was mentioned in the manuscript that the double-dip pattern of the total Q factor can be entirely altered, especially when the system lies deep in the leakage dominated region. This is shown next, in Fig. S1.B, where the three systems previously shown in Fig. 3 are examined here for two scatterer strengths of permittivity $\varepsilon_{r,scat} = 2.5$ and $\varepsilon_{r,scat} = 4.5$. While for the large system of $N = 100$ unit cells the Q factor quickly recovers the double-dip pattern as the scatterer strength increases, in the other extreme of $N = 10$ the Q factor exhibits inverted features which persist with increasing scatterer strength.

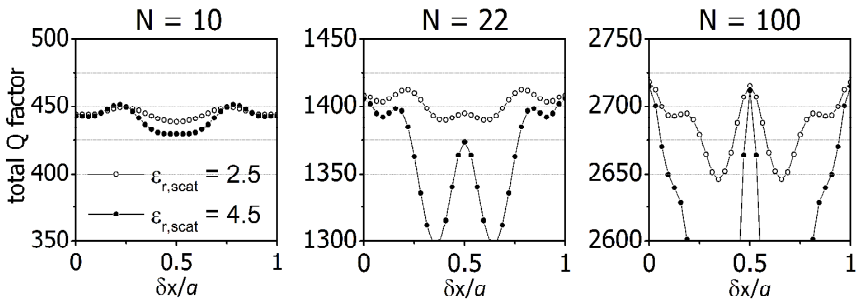

Figure S1.B: Q factor tunability for finite systems of N unit cells with weak scatterer, in the presence of leakage. The scatterer has a 30nm × 60nm rectangular cross section and permittivity $\varepsilon_{r,scat}$ = 2.5 (very weak scatterer, open connected dots) and $\varepsilon_{r,scat}$ = 4.5 (slightly stronger scatterer, filled connected dots). For N = 10, where leakage is stronger than the scatterer outcoupling, the total Q factor shows inverted behavior.

2. Calculation of camera images and far-field angular distributions of the TE_{20} dark and bright modes (system suspended in air)

In Fig. 4 of the main manuscript we examined only the 1st order dark TE_{20} mode in the system proposed for experimental demonstration at 1.5μm under different outcoupling strengths. Here, we show the distinct features of the 1st order dark TE_{20} mode, compared to other orders and, in particular, to the equivalent bright TE_{20} version, which resides at the top of the gap. *Here we do not introduce any scatterers and, hence, the images correspond only to leakage.* To do so, we return to the simpler system examined in Figs. 1-3 and we verify that the conclusions drawn here are the same for the system of Fig.4, which is placed on a substrate with metal on top of the dielectric slab, rather than embedded. In the top panel of Fig. S2 the location of the modes in the dispersion diagram for a system with N = 100 unit cells is illustrated and the respective images are shown in the bottom panel. It is evident, that the leakage leads to distinct patterns for the 1st order TE_{20} mode. For example, the 1st order bright TE_{20} mode shows a single lobe, which does not change qualitatively once the scatterer is introduced (not shown here). On the other hand, we have seen that for the dark TE_{20} mode, the appearance of a single lobe requires strong scatterers (see Fig. 4e). The introduction of scatterers turns a dark mode into bright and this can be identified in the far-field pattern in a unique way.

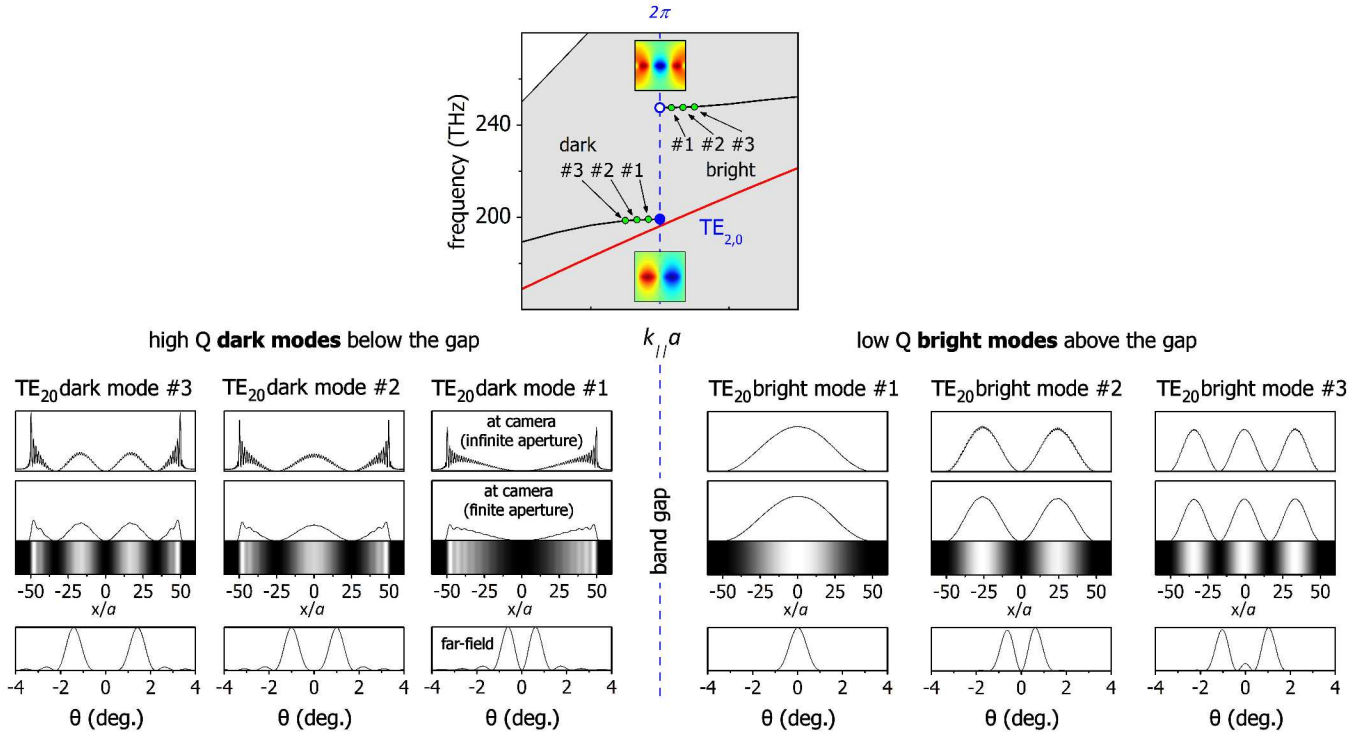

Figure S2: Top: Detail of dispersion diagram close to the 2nd bandgap, showing the first three discrete dark and bright TE_{20} modes. Bottom: Camera images and far-field angular distributions of the first three dark and bright TE_{20} modes around the gap for a system of N = 100 unit cells. The system does not contain any scatterer and, hence, the images depict the effect of leakage only.

3. Metal embedded and metal on top of the dielectric slab

In Fig. 4 in the main manuscript we presented the camera images and far-field distributions for a system on a substrate with the metal interruptions placed on top of the dielectric slab, rather embedded. To demonstrate that the actual placement of the metal does not qualitatively alter the results, here we return to the system suspended in air (a = 960nm, d = 60nm) to complete the analysis and examine both cases (top and middle row panels in Fig. S3). For comparison we also perform the same calculations for the system on a substrate (bottom row panels in Fig. S3), as presented in Fig. 4 (a = 860nm, d = 60nm).

To study the first three dark TE_{20} modes for a system with N = 100 unit cells we choose a scatterer as in Fig. 3 (30nm × 60nm rectangular cross section and permittivity 12.1) and scan the scatterer position δx. For each normalized δx/a we place a density plot slice in the same panel, forming panels that demonstrate the images along the normalized axis x/a for all possible scatterer positions. *To emphasize the structural details of the images, we normalize all slices on the same scale*. Clearly, the images show great qualitative resemblance. For the system on a substrate, in particular, (bottom row panels) the images marked with the red box correspond to the cases shown in Fig. S2 below the gap. Here, although a scatterer is present, it has been placed exactly in the middle, completely suppressing outcoupling. Last, the case marked with the big blue box corresponds to the 1st order dark TE_{20} mode, which is examined in the main manuscript. For the case where the metal is placed on top (middle and bottom row panels), we stop the scan before the δx/a = 0, 1 limits, to avoid overlapping the dielectric scatterer with the metal.

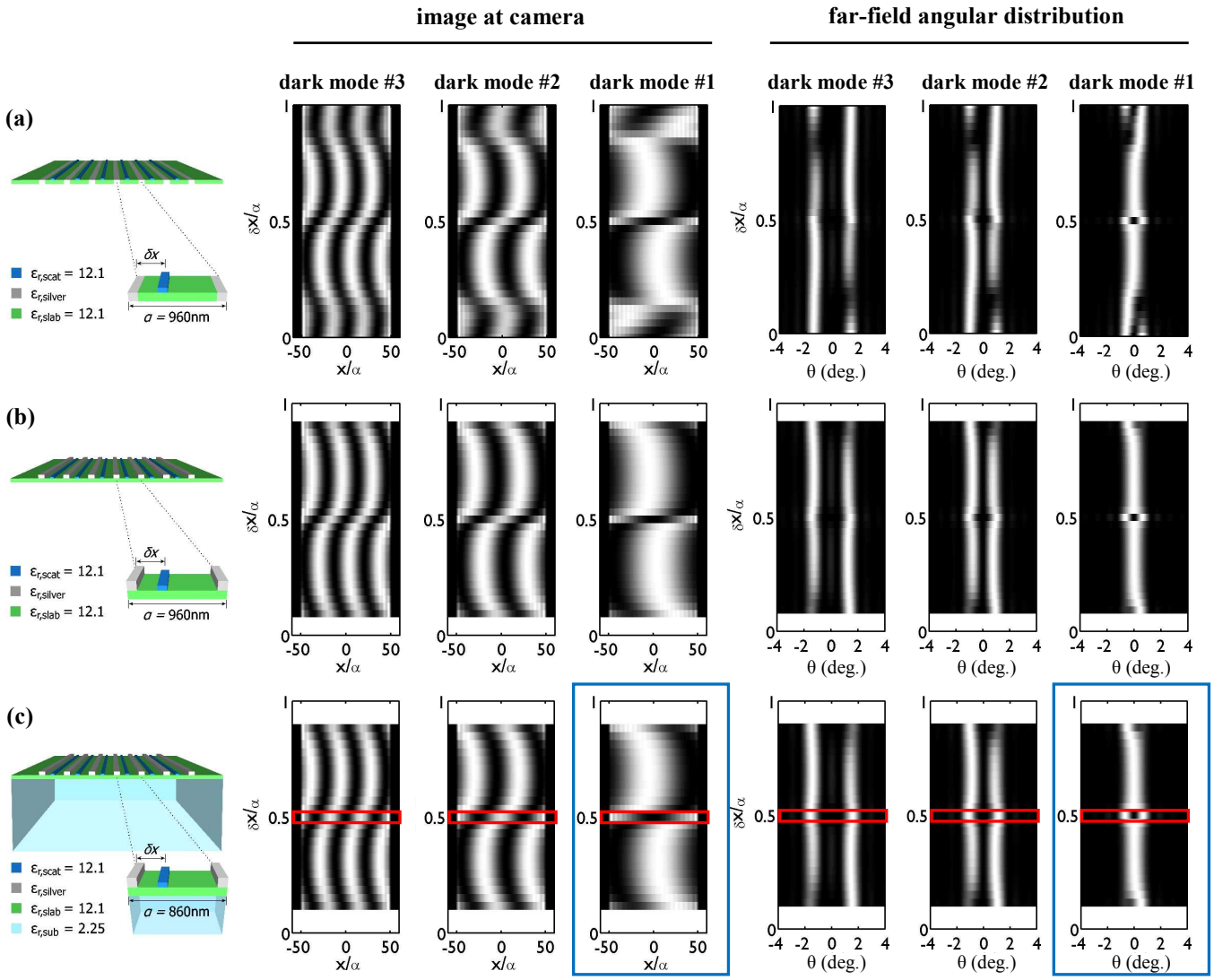

Figure S3: The horizontal slices show the camera image and far-field angular distribution as a function of the scatterer position (out-coupling) on the vertical axis for a system with N = 100 unit cells. In (a) the metal is embedded and in (b), (c) it is located on top of the dielectric slab. In (c) the system has been placed on a substrate and the unit cell size has been reduced to 860nm to maintain the same operation frequency. The images marked with the red box correspond to the cases shown in Fig. S2 below the gap. The case marked with the big blue box corresponds to the 1st order dark TE_{20} mode, which is examined in the main manuscript.

4. Avenues to experimental implementation and proposed structure for lasing in the visible

As previously examined in [3], putting the metasurface on a substrate does quantitatively modify some operation aspects, but does not change the underlying principle physical behavior. Therefore the system can be redesigned for fabrication in a realistic configuration, with predictable performance. For operation at telecom wavelengths, quantum wells [32,33] are very attractive as gain media, not only because they are nowadays very easily available, but because they can serve as the actual dark mode resonator (slab with gain), making a compact source. Alternatively, a p-n junction can serve as the slab with gain [S1], offering direct integration with other optoelectronic components, as it requires electrical, instead of optical pumping. Another option is to use quantum dots as gain material [S2,S3], which can be placed on top of the dielectric slab, dispersed in a host matrix, such as certain polymers [S4]. This configuration, in particular, could be attractive for optical systems, where gain can be implemented with emitting dyes [S5,S6]. So, although both will work theoretically at any frequency, the former system with quantum wells (or doped semiconductors) is interesting for telecommunication wavelengths and the latter system, although it can be made work in the infrared with the use of quantum dots, opens the path for implementation at optical frequencies using dyes. The system examined in this paper falls within the first major category and is shown in Fig. S4a in a realistic implementation, in which it has been placed on a glass substrate. In fact, the slab permittivity considered in this work (12.1) corresponds to an average permittivity of typical $In_xGa_{1-x}As/Al_yIn_{1-y}As$ quantum wells [S7]. Due to the presence of the substrate, the refractive step index between the slab and its environment reduces and the dark mode frequency drops. In order to restore operation at 1.5μm, the unit cell size is reduced to 860nm, while all other parameters remain the same. To simplify the fabrication process the system is designed to operate with metal wires placed on top of the dielectric slab, instead of interrupting it [3]. Fabrication can be further facilitated, as simulations verify that the dielectric slab does not have to be truncated at the end of the finite structure of length L, but can extend across the whole substrate. In this case, the boundaries of the finite structure are set by the edge metal stripes.

For lasing in the visible, emitting dyes dispersed in polymers such as PMMA can be placed as a superstrate, as shown in Fig. S4b. When the gain is placed on top of the slab, in order to achieve the largest interaction possible between the dark mode and gain, it is preferable that the dark mode extents as much as possible outside the slab region. To achieve the largest spatial extent of the dark mode, the slab thickness and refractive index should be as low as possible. However there is a trade-off, because the less confined the dark mode, the more its dispersion line approaches the substrate lightline. This is generally undesirable, as the slightest material or fabrication irregularity could push the dark mode into the substrate region. Along these lines, for the proposed structure of Fig. S4b, which is designed to operate at 570nm (emitting green light), a 60nm thin HfO_2 slab is considered. At this wavelength the permittivity of thin film HfO_2 is 4.2 and of bulk Ag is ~ –12.0–1.0i. The metal is less reflective and more absorptive than in the infrared and, as a consequence, leakage is more intense. Hence, either more unit cells will be needed to reach the performance of the infinite system or strong enough scatterers should be considered, in order for the outcoupling to dominate leakage.

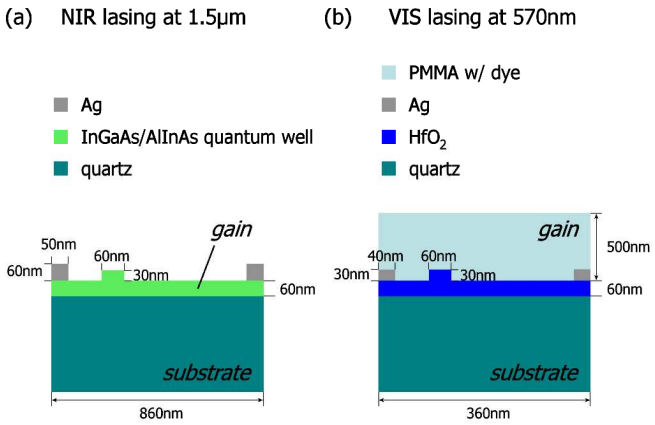

Figure S4: Realistic systems on a substrate, proposed for operation at (a) 1.5μm and (b) 570nm.

5. Proposed system for operation at 1.5μm: system on a substrate with metal placed on top of the dielectric slab

Here we give some additional information about the system proposed for lasing at 1.5μm. For the infinite system, the band structure of the TE_{20} mode is shown in Fig. S5a and, for a finite system of $N = 100$ unit cells, the image at camera and far-field angular distribution of the 1st dark TE_{20} mode as a function of the scatterer permittivity $\varepsilon_{r,scat}$ is shown in Fig. S5b. *Here the images have been normalized according to the maximum radiated power for each position of the scatterer, to emulate the expected intensity variation.* For $\varepsilon_{r,scat} = 12.1$, in particular, the results have been reproduced from Fig. S3 (case marked with the big blue box) according to the new normalization.

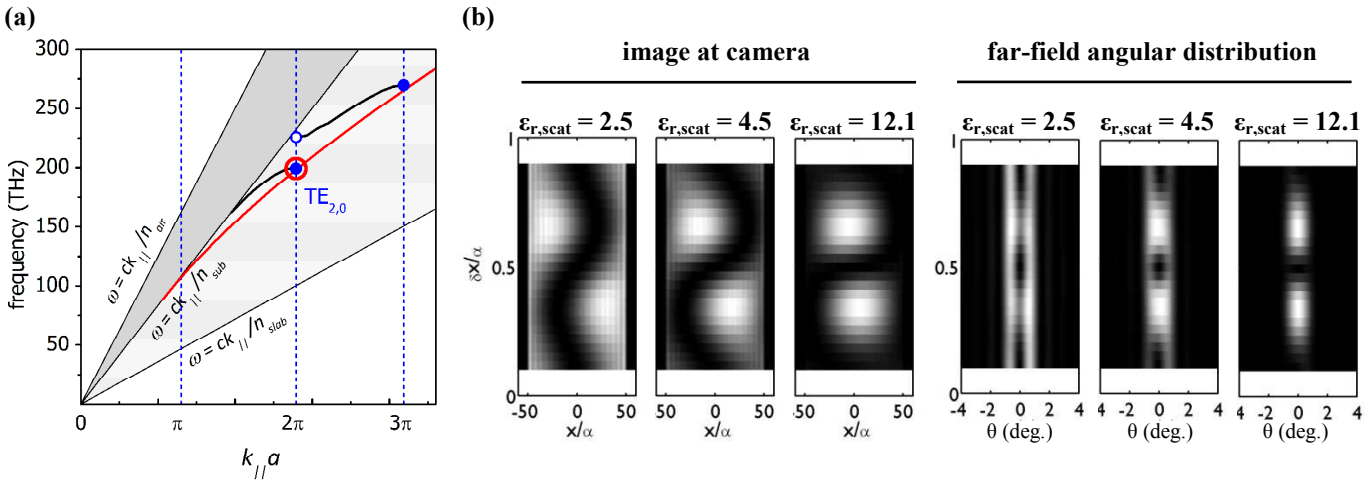

Figure S5: (a) Band structure of TE_0 and (b) effect of scatterer's strength on camera image and far-field angular distribution (mode #1). The TM_0 branch has a cutoff at 340THz and is therefore not visible in (a).

In Fig. S6 patterns of the $m = 1$ order TE_{20} mode are shown for a system with $N = 100$ unit cells, as the outcoupling strength increases. To facilitate fabrication, we have placed a single scatterer on top of the gain slab. As a result, the absence of a secondary scatterer that can enable full control over the emission direction, leads most of the outcoupled power to be directed towards the substrate.

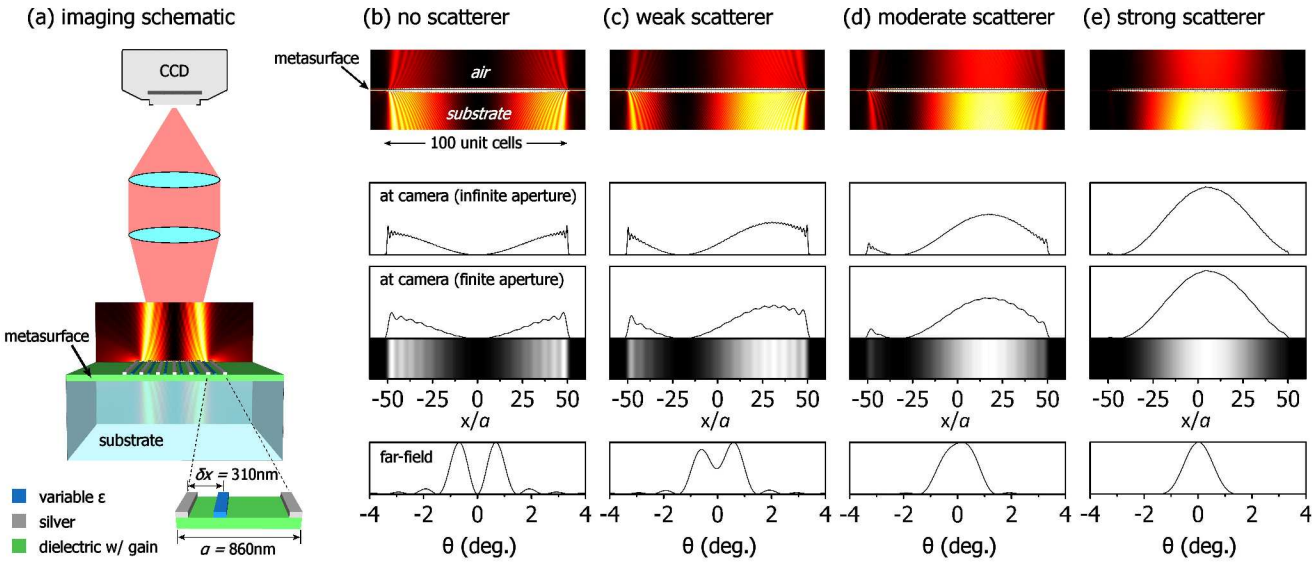

Figure S6: Intensity patterns due to leakage of the 1st order dark mode for a system with $N = 100$ unit cells, for different outcoupling strengths. The scatterer has a 30nm × 60nm rectangular cross section and its outcoupling strength is tuned via its permittivity, which is set to 1 in (b), 2.5 in (c), 4.5 in (d) and 12.1 (e). The top row shows a saturated colormap of $|E_z|^2$ at the vicinity of the metasurface, which is located horizontally in the middle of the panel. The actual dark mode distribution is not visible due to the saturated colormap. The image seen with a camera is shown in the two middle rows, for ideally infinite aperture and realistically finite aperture (shown as density plot as well). The bottom row shows the far-field angular distribution.

In Fig. S7 an additional scatterer has been placed below the metasurface to boost directionality (ratio of power going into the air vs power going into the substrate) towards the superstrate region, according to the ideas presented in [2]. The dot marks the operation point, for which the performance is depicted in Fig. 4 of the main manuscript.

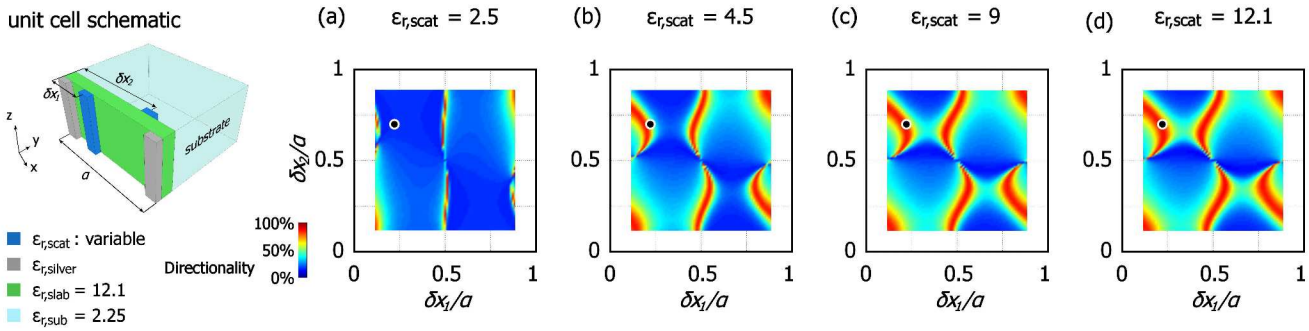

Figure S7: Directionality in a double scatterer configuration for variable scatterer strength.

References

[S1] Sze, S. M. & Ng, K. K. Physics of Semiconductor Devices (John Wiley & Sons, New Jersey, 2007).

[S2] Plum, E., Fedotov, V. A., Kuo, P., Tsai, D. P. & Zheludev, N. I. Towards the lasing spaser: controlling metamaterial optical response with semiconductor quantum dots. Opt. Express 17, 8548–8551 (2009).

[S3] Tanaka, K., Plum, E., Ou, J. Y., Uchino, T. & Zheludev, N. I. Multifold Enhancement of Quantum Dot Luminescence in Plasmonic Metamaterials. Phys. Rev. Lett. 105, 227403 (2010).

[S4] Riechel, S., Kallinger, C., Lemmer, U., Feldmann, J., Gombert, A., Wittwer, V. & Scherf, U. A nearly diffraction limited surface emitting conjugated polymer laser utilizing a two-dimensional photonic band structure. Appl. Phys. Lett. 77, 2310–2312 (2000).

[S5] Wuestner, S., Pusch, A., Tsakmakidis, K. L., Hamm, J.M. & Hess, O. Overcoming losses with gain in a negative refractive index metamaterial. Phys. Rev. Lett. 105, 127401 (2010).

[S6] Xiao, S., Drachev, V. P., Kildishev, A.V., Ni, X., Chettiar, U. K., Yuan, H.-K. & Shalaev V. M. Loss-free and active optical negative-index metamaterials. Nature (London) 466, 735–738 (2010).

[S7] Mondry, M. J., Babic, D. I., Bowers, J. E. & Coldren, L. A., Refractive Indexes of (Al, Ga, In)As Epilayers on InP for Optoelectronic Applications, IEEE Photon. Tech. Lett. 4(6), 627 1992.